Performance Investigation of Modulation Format Identification in Super-Channel Optical Networks

Waddah S. Saif, Amr M. Ragheb, Bernd Nebendahl, Tariq Alshawi, *Senior Member, IEEE*, Mohamed Marey, *Senior Member, IEEE*, and Saleh A. Alshebeili

***Abstract*—The problem of automatic modulation format identification (MFI) is one of the main challenges in adaptive optical systems. In this work, we investigate MFI in super-channel optical networks. The investigation is conducted by considering the classification of seven multiplexed channels of 20 Gbaud, each with six commonly used modulation formats, including polarization division multiplexing (PDM)-BPSK, PDM-QPSK, and PDM-MQAM with (M = 8, 16, 32, 64). The classification performance is assessed under different values of optical signal-to-noise ratio (OSNR) and in the presence of channel interference, channel chromatic dispersion, phase noise, and 1st polarization mode dispersion (PMD). Furthermore, the effect of fiber nonlinearity on the MFI accuracy is investigated. A well-established machine learning algorithm based on histogram features and a convolutional neural network has been used in this investigation. Results indicate that accurate identification accuracy can be achieved within the OSNR range of practical systems and that the MFI accuracy of side subcarriers outperforms that of middle subcarriers at a fixed value of OSNR. The results also show that the MFI accuracy of PDM-16QAM and PDM-64QAM are affected more by channel interference than the other modulation formats, especially when the ratio of the subcarrier bandwidth to subcarriers spacing is $\geq$ 1.4. Finally, laboratory experiments have been conducted for validation purposes. The experimental results were found in good agreement with those achieved by simulation.**

***Index Terms*—Machine learning, modulation format identification, super-channel optical networks.**

I. Introduction

THE ever increasing demand of high speed applications such as internet protocol (IP) video delivery, cloud computing, and internet-of-everything put a great challenge on the existing optical networks [1]. Much efforts have been spent during the last years in order to increase the spectral efficiency (SE) of the current optical networks [2]. These include efficient bit, wavelength, and space multiplexing. Optical super-channel is one of the promising solutions that reduces inter-channel guard-bands, which leads to laying out wavelength channels on flexible grids or gridless structure, instead of conventional fixed wavelength spacing [3], [4]. In this respect, super-channel has been recognized as a potential technology for optical networks with 400 Gbps and 1 Tbps data capacity [5]. It mitigates the bandwidth restrictions of optoelectronic devices by creating multi-subcarriers from a single optical source. These subcarriers are combined together to achieve high transmission capacity (i.e., high SE).

Beside increasing capacity, future optical networks such as elastic optical networks are expected to be more adaptive and cognitive [6], [7]. These kinds of networks have the capability to dynamically change data rate, modulation format, transmission wavelength, and signal power, *etc.* according to different link conditions and quality of service requirements. Accordingly, it is no longer guaranteed that the signals arriving at the receiver side/network nodes would have the same modulation format. In this regard, automatic modulation format identification (MFI) will be a common need for the future optical fiber networks as it can provide the network more autonomy and flexibility [8].

Over the last years, several MFI techniques for single mode fiber (SMF)-based networks have been proposed. For instance, an MFI technique based on comparing normalized reference signals (i.e. M-ary quadrature amplitude modulation (M-QAM)) with the normalized amplitude of received signal has been proposed in [9]. Similarly, MFI method based on amplitude histogram entropy has been given in [10]. In this technique, the entropy of amplitude histogram is utilized to distinguish between the different modulation formats. These techniques are tolerant to phase noise (PN) and frequency offset, and can only distinguish M-QAM signals. In [11], the authors proposed MFI based on the peak-to-average-power ratio (PAPR) parameter, which is extracted from the normalized power distribution. This algorithm is easy to implement; however, it requires a high OSNR to provide high MFI accuracy. Also, in [12], the PAPR is evaluated from the frequency domain of the received signal after performing different nonlinear operations. This method shows a high computational complexity owing to the nonlinear power operations [13]. Besides, an MFI scheme based on intensity profile features has been proposed in [14], where the intensity

Manuscript received December 17, 2021; revised January 20, 2022; accepted January 31, 2022. Date of publication February 7, 2022; date of current version February 18, 2022. This work was supported by the Deputyship for Research and Innovation, Ministry of Education in Saudi Arabia under Grant DRI-KSU-1088. *(Corresponding author: Waddah Saif.)*

Waddah S. Saif, Tariq Alshawi, and Saleh A. Alshebeili are with the Electrical Engineering Department, King Saud University, Riyadh 11421, Saudi Arabia, and also with the KACST-TIC in Radio Frequency and Photonics for the e-Society, King Saud University, Riyadh 11421, Saudi Arabia (e-mail: waddah.alkhulidy@gmail.com; talshawi@ksu.edu.sa; dsaleh@ksu.edu.sa).

Amr M. Ragheb is with the KACST-TIC in Radio Frequency and Photonics for the e-Society, King Saud University, Riyadh 11421, Saudi Arabia (e-mail: aragheb@ksu.edu.sa).

Bernd Nebendahl is with the Keysight Technologies, 71034 Boeblingen, Germany (e-mail: bernd_nebendahl@keysight.com).

Mohamed Marey is with the Smart Systems Engineering Laboratory and College of Engineering, Prince Sultan University, Riyadh 11586, Saudi Arabia (e-mail: mfmmarey@psu.edu.sa).

Digital Object Identifier 10.1109/JPHOT.2022.3148798

profile features can be obtained using Fourier curve fitting of the amplitude histogram. Note that the previously mentioned methods do not need prior training data, but they are highly sensitive to pre-defined threshold values.

On the other side, machine learning (ML) algorithms have been utilized in several fields and shown to present superior results compared to conventional digital signal processing (DSP) approaches. In fiber optical networks, there have been extensive works on the use of ML, as in routing optimization [15], fiber nonlinearities mitigation [16], optical performance monitoring (OPM) [17], [18], and MFI [8]. In MFI, the authors in [19], [20] proposed an identification technique based on artificial neural network (ANN) and amplitude histogram (AH) to identify different optical modulation formats. Though this method does not require timing recovery and additional hardware/circuits, it is not appropriate for classifying the high order modulation types (i.e. M-QAM, $M > 16$). Other MFI techniques that consider the pixel points of an image extracted from received data were considered in [21], [22]. For example, the constellation [21] and eye diagram [22] images were used as input to convolutional neural network (CNN). Additionally, Radon transform (RT) of the constellation diagram was proposed in [23]. These techniques can achieve precise results; however, dealing with images might increase the computational cost. For polarization division multiplexing (PDM) transmission, the received signal can be expressed by Stokes parameters. The various modulation formats can be identified according to number of clusters in Stokes space. Different clustering algorithms, such as Gaussian mixture model (GMM) [24], connected component analysis [25], and clustering by fast search and find of density peaks (CFSFDP) [26] have been utilized. Instead of using clustering algorithms in Stokes space, the authors in [27] exploited the constellation diagrams of the different modulations and used them as input images to CNN. Meanwhile, the authors in [28] used both AH and constellation images with two consecutive probabilistic neural network (PNN) algorithms to identify different modulation formats. In [29], the authors proposed an MFI technique based on deep neural networks (DNNs) in conjunction with features extracted from received signals' density distributions in Stokes axes. It is worth noting that Stokes parameters are entirely free of phase noise, frequency offset, and state of polarization. However, Stokes space constellations suffer from polarization mode dispersion and polarization dependent loss [30]. In addition, the authors in [31] investigated ML-based MFI in few mode fiber (FMF)-based optical networks.

So far, and to the best of authors' knowledge, MFI has not been yet considered in literature for super-channel optical networks. Therefore, this work contributes to the field of optical communications by filling this gap. In particular,

1) We investigate the MFI in super-channel network under the effect of different channel impairments, including channel additive noise, chromatic dispersion (CD), PN, PMD, fiber nonlinearity, and channel interference resulting from the simultaneous transmission of different signals over the channel. Our investigation is equipped with a well-established ML algorithm; a CNN classifier trained with the two-dimensional (2D) in-phase quadrature histogram (IQH) features. We selected such a technique for our investigation because the 2D-IQH and/or CNN have been effectively used in literature for MFI in other types of optical channels; e.g. single mode fiber, few mode fiber, and free space optical channels; see [8] and the references therein.
2) We investigate the MFI for different and widely used modulation formats. For the sake of conducting laboratory experiments and performing simulations, we consider the MFI for a super-channel having seven $\times$ 20 Gbaud multiplexed signals with PDM-BPSK, PDM-QPSK, PDM-8QAM, PDM-16QAM, PDM-32QAM, and PDM-64QAM schemes. We study the effect of super-channel inter-carrier interference on the MFI performance. To avoid redundancy, the MFI accuracy is reported for two optical subcarriers, one in the middle (i.e., the middle of the seven utilized subcarriers) of the spectrum and the other at the edge. We assess the identification performance under OSNR values ranging from 8 to 38 dB. Moreover, we address the effect of fiber CD at 400 ps/nm and 800 ps/nm, laser PN at 10 kHz and 1000 kHz, and 1st polarization mode dispersion (PMD) at differential group delay (DGD) ranging from 5 to 50 ps, and a state of polarization (SOP) angle of 5° and 25°. Furthermore, the effect of fiber nonlinearity on the MFI accuracy is investigated. We also demonstrate experimental results for validation purposes..

The paper is organized as follows. Section II introduces the concept of super-channel in optical networks. Section III introduces the MFI technique utilized in this investigation. Section IV is concerned with the simulation investigation, where the simulation setup, data generation, and simulation results of MFI technique are presented and discussed. The experimental validation is given in Section V. Concluding remarks are given in Section VI.

II. Concept of Super-Channel

In wavelength division multiplexing (WDM) network, multiple wavelengths are employed to transmit data via fiber channel in a parallel manner. However, the gaps between various channels lead to waste in spectral resources and decrease in system throughput. Meanwhile, fixed grid transmission is no longer able to operate with high traffic demands beyond 100 Gb/s. Super-channel has been proposed to reduce/remove the gabs between optical carriers, hence improving SE. Super-channel transmission was firstly used as multi single-carrier-modulated signals, similar to orthogonal frequency-division multiplexing (OFDM) [32]. Later, the concept of super-channel was generalized to any set of carriers modulated, multiplexed, transmitted, and routed together over the same optical channel. Super-channel transmission can even be used for signals that are not typically bundled together. The International Telecommunication Union (ITU) has recently standardized the use of super-channel under the terminology "flexible grid WDM" [33].

The super-channel configuration can be classified into three types, according to the interference ratio (η), define as the ratio

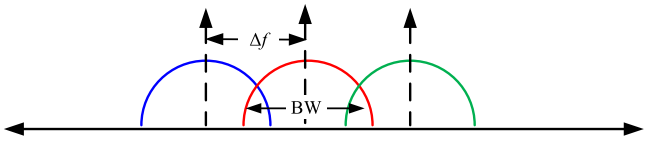

Fig. 1. Super-channel with interference ratio, $\eta = \mathrm{BW}/\Delta f > 1$.

of the subcarrier bandwidth (BW) to subcarriers spacing (Δf). In the first type, $\eta < 1$, the spacing between the subcarriers is greater than the subcarrier bandwidth and hence no interference is present. This type is similar to the traditional WDM system. In the second type, $\eta = 1$, the subcarrier spacing is equal to the subcarrier bandwidth. The third type, $\eta > 1$, is the most challenging configuration where the subcarriers overlap, and the spacing between them is eliminated. Hence, inter-carrier-inference (ICI) occurs (see Fig. 1) and advanced DSP is needed to eliminate ICI effect [34].

Super-channel based optical networks can provide transmission speed up to tens of Tb/s [5]. In this respect, research records of super-channel demonstrations with a capacity of tens of Tera-bits have been reported in literature. For instance, terabit super-channel transmission system, comprising 10×120-Gb/s PDM-QPSK, was experimentally demonstrated in [35]. The transmission distance reached 10,000 km and 9,000 km with interference ratios of 1.1 and 1, respectively. Using higher order modulation formats (e.g., PDM-256QAM), 50 × 24 Gbaud comb-based super-channels with overall SEs of 11.5 b/s/Hz [36] and 12 b/s/Hz [36] have been demonstrated to achieve throughputs of 44.7 Tb/s and 45.6 Tb/s, respectively. Furthermore, 7 × 201 super-channel transmission over 7,326-km is experimentally investigated in [37]. The transmission speed and capacity-distance product reached 140.7-Tbit/s and 1.03 Exabit/s· km, respectively.

III. MFI Based on 2D-IQH Features and CNN

In this section, we consider the 2D-IQH with CNN for MFI. Unlike the constellation-based scheme that relies on images [21], [22], the 2D-IQH forms densities by combining both the in-phase (I) and quadrature (Q) information on a 2D histogram (i.e. the number of joint occurrences of I and Q values) [17], [31], [38]. The 2D-IQH is the output of step 2, as described in Fig. 2(a). In the third step, IQH gets converted to images just for visualization. The 2D-IQH provides a statistical distribution related to both the amplitude and phase information of the received signal. This advantage makes it excels compared with other features such as the AH [14] and the cumulative distribution function (CDF) [39] that only exploit the signal's amplitude. In addition, the IQH can work with machine learning algorithms that accept 2D input, such as CNN. In Fig. 2(b), we display the IQH of BPSK, QPSK, 8QAM, 16QAM, and 64QAM. It is obvious that all modulation formats have different IQHs. However, the presence of high amplified spontaneous emission (ASE) could change the IQH shape of some modulations such as the 16QAM and 64QAM. In this case, misclassification between these modulation formats might occur.

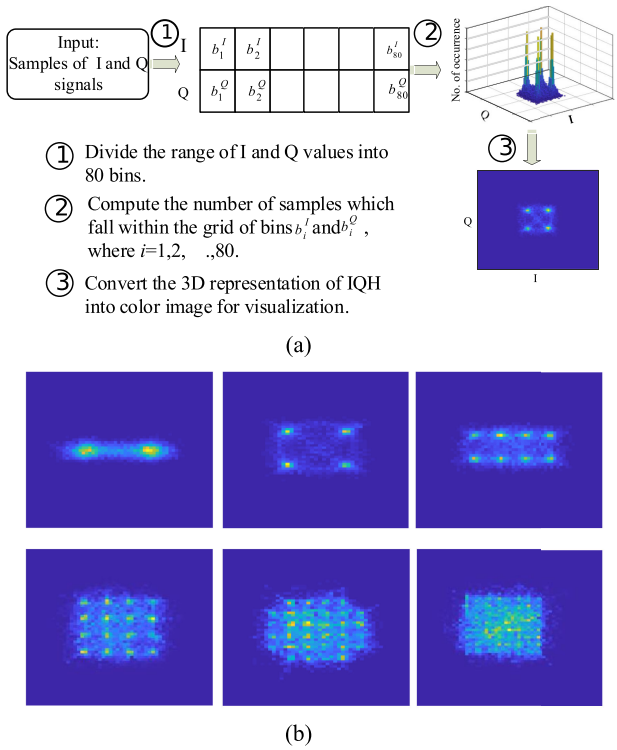

Fig. 2. (a) The concept of generating IQH, and (b) The IQH of different modulation formats: 1st row (BPSK, QPSK, and 8QAM, respectively) and 2nd row (16QAM, 32QAM, and 64QAM, respectively).

The CNN, on the other hand, is considered as a special type of DNNs which are effectively dealing with 2D problems [21]. Basically, it consists of different layers including, convolutional, pooling, and fully connected neural networks, as shown in Fig. 3. For each convolutional layer, the input images are convolved with kernel filters to produce the feature maps. The pooling layer reduces the size of the feature map from one layer to another in the network using either 2 × 2 average or max filter. This combination of convolution and pooling operations is possibly repeated more than one time. The last layer is a fully connected layer that maps the extracted features to the desired outputs. The fully connected layer is a special kind of activation layer, called softmax, which converts a vector of numbers into a vector of probabilities. The rectified linear unit (ReLU) is used in our work as an activation function. The error between the predicted and target classes is calculated using the cross-entropy loss function (L) [40]. The loss (L) is back-propagated to adjust the network parameters (e.g. weights and bias) through a training process. Since the CNN network is more effective with inputs of 2D type, in this work, the in-phase and quadrature components of the received signal are combined together to produce a 2D histogram that is used as an input to the CNN network.

An essential step for designing an ML network is to choose an appropriate set of hyperparameters, well-suited for the application at hand. In our work, we have considered different CNN hyperparameters by varying (number of layers, number of kernel filters per layer, filter's size, number of hidden layers, learning rate, etc.). In particular, the number of layers is varied

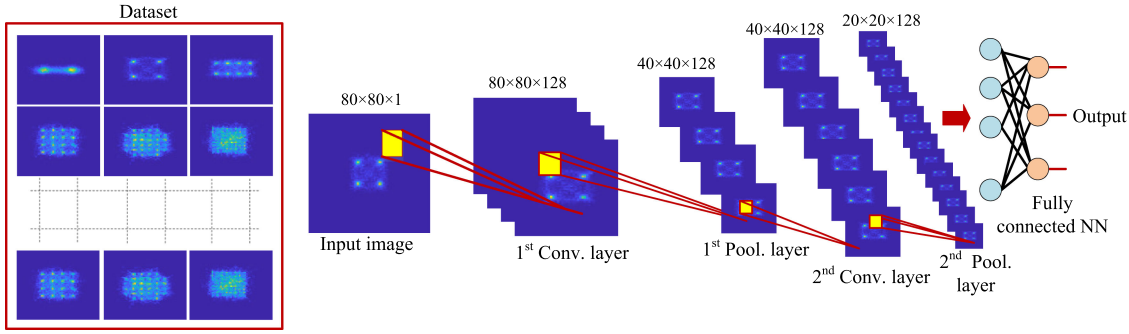

Fig. 3. The schematic diagram of CNN network.

TABLE I
HYPERPARAMETERS OF PROPOSED CNN

Hyperparameter	Value
Number of layers	2
Number of filters per layer	128
Filter size	3×3
Learning rate	0.001
Mini-batch size	128
L2 regularization	0.001
Optimizer	Adam
Max. Epoch number	100

TABLE II
FIBER PARAMETERS USED IN THE SIMULATION

Parameter	Value
Dispersion coefficient	16×10^{-6} s/m^2
Dispersion slope	0.08×10^{3} s/m^3
Nonlinear coefficient	2.6×10^{-20} m^2/W
DGD	$(5 - 50)\times10^{-12}$ s
SOP	5° & 25°

to take on the values 1,2, and 3; number of kernel filters to be 8, 16, 32, 64, and 128; and number of hidden layers in the fully connected neural network to be 0, 1, 2. Further, we adjusted the learning rate on a logarithmic scale ranges from 1 to 1×10^{-6}. Then, we selected the best settings for these parameters which have minimum validation cross-entropy loss. On the other hand, $L2$ regularization is used to prevent CNN from over-fitting. Finally, a mini-batch (i.e. splitting the training data into small batches), with batch normalization (i.e. subtracting the mean of each batch and dividing by the batch standard deviation), is used to normalize each input channel. The utilization of this operation is to speed up the training of the CNN network as well as to increase its robustness to bad initialization of weights [41]. Table I summarizes the hyperparameters used in this work.

IV. SIMULATION INVESTIGATION

In the following subsections, we present the simulation setup utilized in our investigation and description of generating the training and testing datasets. Then, we present the results of our investigation with discussion.

A. Simulation Setup

The simulation setup is shown in Fig. 4, where a 7×20 Gbaud super-channel system is built using VPI transmissionMaker. In this setup, all channels transmit data simultaneously using the same modulation format. For each subcarrier, six commonly used modulation formats including PDM-BPSK, PDM-QPSK, PDM-8QAM, PDM-16QAM, PDM-32QAM, and PDM-64QAM at symbol rate 20 Gbaud are generated. The optical source of each subcarrier is a continuous wave (CW) laser. The central subcarrier operates at 1550 nm wavelength, while the wavelength of other subcarriers is adjusted according to the value of η. A WDM multiplexer is used to combine the different subcarriers. The multiplexed signals are transmitted through a standard single-mode fiber (SSMF). The fiber length is adjusted in order to obtain different CD values. The fiber parameters used in the simulation are summarized in Table II. Optical band pass filter (OBPF) with 50 GHz bandwidth is used to select one of the seven channels. An erbium-doped fiber amplifier (EDFA) with variable optical attenuator (VOA) is used to control the ASE noise added to the optical signal. At the receiver side, the two polarized signals are separated using polarization beam splitter (PBS), then optical demodulation is carried out by mixing the received optical signal with a local oscillator. After that, balanced detectors with hybrid 90° is employed to convert the optical signal into electrical waveforms. Two analog-to-digital converters (ADCs) are used to obtain I and Q samples. The resultant samples for each I and Q, with length 8192, are further utilized to build IQH, after normalization using standard deviation. The normalized 2D-IQH features is used as input to the CNN classifier.

B. Data Generation

This subsection describes the generation of training and testing datasets. As we discussed in Section II, the optical networks can be classified into three types according to the value of η. In this work, we limit our study to the third type (i.e. $\eta > 1$),

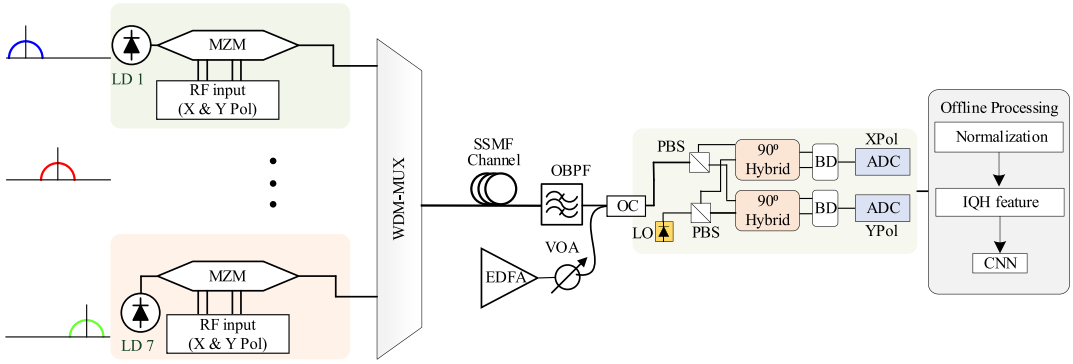

Fig. 4. Simulation setup of the proposed MFI in super-channel networks. LD: laser diode, MZM: Mach-Zehnder modulator, MUX: multiplexer, DE MUX: de-multiplexer, EDFA: Erbium-doped fiber amplifier, VOA: variable optical attenuator, WDM: wavelength division multiplexing, OBPF: optical band pass filter, PBS: polarization beam splitter, BD: balanced detector, ADC: analog to digital convertor, LO: local oscillator, IQH: in-phase quadrature histogram, CNN: convolutional nureal network.

which is more challenging. We consider four interference values in the range of 1.1 to 1.4 with 0.1 step size; this is equivalent to a SE range from 9.6 to 11.8 b/s/Hz utilizing PDM-64QAM. For each interference value, a dataset pool of 9600 histograms is created using 100 independent realizations for each of the six modulation types. All modulations are generated with 16 different OSNR values, from 8 to 36 dB in step of 2 dB. 70% of the total dataset is randomly selected for training while the remaining 30% of the dataset is used for testing.

In the next subsection, we discuss the MFI accuracy results of 7×20 Gbaud super-channel system. Since the system subcarrier is either in the middle where it overlaps with two neighbor subcarriers, or at the side(edge) of the spectrum where it overlaps with only one subcarrier, we limit our study to one of each type to avoid redundancy. We show the identification accuracy results at different values of η and presence of other impairments such as ASE noise, CD, and PN.

C. Results and Discussion

In this subsection, we present the results of our investigation with discussion. Fig. 5 (a and b) ($\eta = 1.1$) shows that the MFI accuracy of PDM-BPSK, PDM-QPSK, PDM-8QAM, and PDM-32QAM, for both side (left-column) and middle (right-column) subcarriers, exceeds 97% at OSNR values $\geq$ 16 dB. Also, for the side subcarrier, the MFI accuracy for PDM-16QAM and PDM-64QAM exceeds 97% at OSNR values $\geq$ 22 dB. However, for the middle subcarrier, at OSNR values $\geq$ 26 dB the MFI accuracy for PDM-16QAM and PDM-64QAM are $\geq$ 97% and $\geq$ 90%, respectively. It can be observed that the performance of the side subcarrier is better than the middle. Further, although the order of PDM-32QAM is higher than that of PDM-16QAM, its classification accuracy is greater than PDM-16QAM. This could be attributed to the high similarity between the IQH diagrams of PDM-16QAM and PDM-64QAM in relatively high impairments, which causes misclassification and degradation in the MFI accuracy for PDM-16QAM and PDM-64QAM, rather than the other modulation types.

Besides, as the value of η increases the MFI decreases. For example, for the middle subcarrier, the OSNR value required

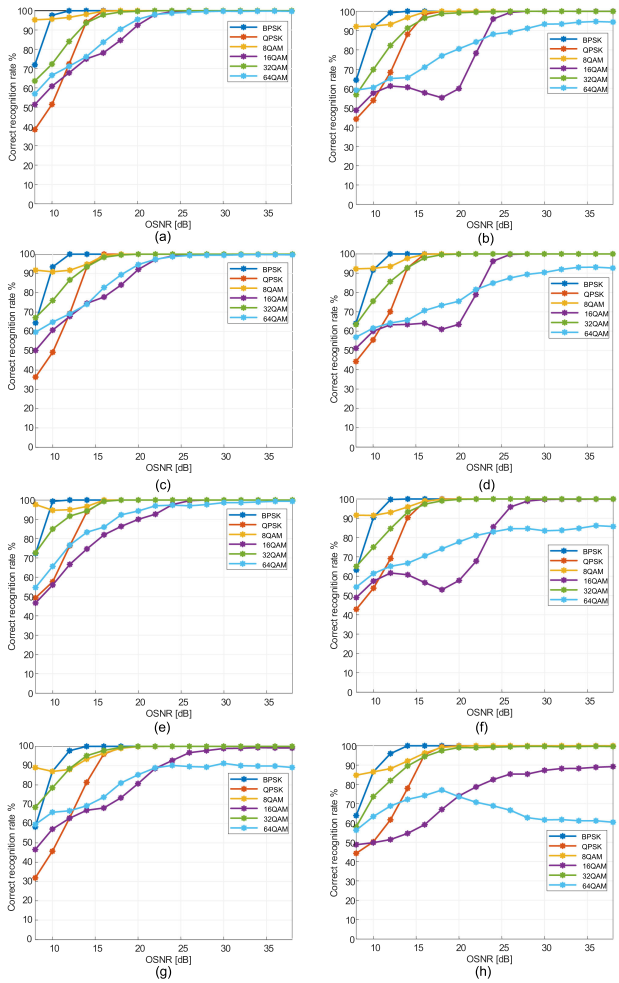

Fig. 5. MFI accuracy for side (1st column) and middle (1nd column) subcarriers vs OSNR at (a and b) $\eta = 1.1$, (c and d) $\eta = 1.2$, (e and f) $\eta = 1.3$, and (g and h) $\eta = 1.4$.

to achieve accuracy $\geq$90, for PDM-64QAM, increases from 26 to 28 dB when η increases from 1.1 to 1.2, as shown in Fig. 5(d). Meanwhile, the MFI accuracy drops below 90% when η increases to 1.3 (see Fig. 5(f)). On the other hand, for the

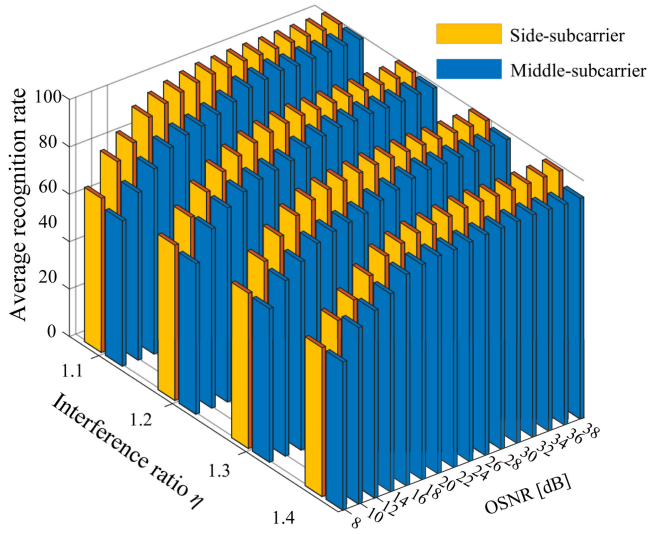

Fig. 6. Average MFI accuracy vs. OSNR for different values of η.

TABLE III
THE REQUIRED OSNR TO ACHIEVE SPECIFIC AVERAGE MFI ACCURACY FOR BOTH SIDE AND MIDDLE SUBCARRIERS AT $\eta = 1.4$

Average MFI accuracy %	Side subcarrier	Middle subcarrier
93	17.31 dB	25.10 dB
98	25.47 dB	–

side subcarrier, the MFI accuracy is almost the same for all modulations when η increases from 1.1 to 1.2. However, there is a slight decrease in MFI accuracy when η increases to 1.3, especially for PDM-16QAM and PDM-64QAM modulation schemes (see Fig. 5(a), (c), and (e)).

The effect of the interference is more noticeable when η reaches 1.4. For the middle subcarrier, both PDM-16QAM and PDM-64QAM are greatly affected. The accuracy of PDM-16QAM becomes around 90% at OSNR values $\geq$30 dB. However, for PDM-64 QAM, the MFI accuracy decreases to around 60%, as shown in Fig. 5(h). While, for the side subcarrier, the MFI accuracy can reach about 90% when the OSNR values exceeds 22 dB, as shown in Fig. 5(g).

Fig. 6 summarizes the average identification accuracy versus OSNR for all considered η values. It is observed that the average MFI accuracy decreases as η increases and increases as OSNR values increases. Meanwhile, the side subcarrier shows better performance than the middle subcarrier. Table III, extracted from Fig. 6, presents the required OSNR for the side and middle subcarriers to achieve average accuracies 93% and 98% at $\eta = 1.4$. Note that the middle subcarrier requires extra 7.79 dB in OSNR to reach the same performance of side subcarrier at an average classification rate of 93%. On the other hand, the side subcarrier achieves an average classification rate of 98% at OSNR = 25.47 dB, while the middle subcarrier fails to reach such performance at this level of interference.

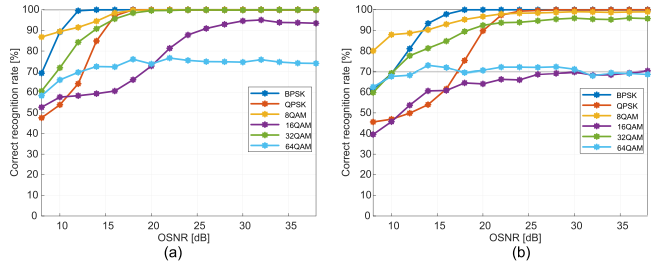

Fig. 7. MFI accuracy vs OSNR at $\eta = 1.1$ in the presence of different CD and PN (a) CD = 400 ps/nm and PN = 10 kHz and (b) CD = 800 ps/nm and PN = 1000 kHz.

The effect of various conditions, including CD and PN, is also addressed. We consider the middle subcarrier (i.e. the more challenging subcarrier) at $\eta = 1.1$. The MFI accuracy versus OSNR values, in the presence of CD = 400 ps/nm and PN = 10 kHz, is shown in Fig. 7(a). It can be noted that the MFI accuracy, for PDM-BPSK, PDM-QPSK, PDM-8QAM, and PDM-32QAM signals, reaches 100% at OSNR equals 20 dB, while the MFI accuracy, for PDM-16QAM and PDM-64QAM, at OSNR values $\geq$ 30 dB are around 95% and 75%, respectively. On the other hand, in the presence of CD = 800 ps/nm and PN=1000 kHz, the system requires 25 dB OSNR to reach 100% MFI accuracy, for PDM-BPSK, PDM-QPSK, and PDM-8QAM, while for PDM-32QAM the performance saturates at 95%; see Fig. 7(b). Also, PDM-16QAM and PDM-64 QAM show the worst accuracy performance among the other modulation formats, where their accuracies decrease to 60% even at the higher OSNR values. It is worth noting that the results presented in Fig. 7 have considered CD values up to 800 ps/nm (i.e., 50 km fiber length) employing the MFI directly after the ADC. If higher CD values corresponding to higher fiber lengths are to be considered, a CD compensation algorithm needs to be used, preceding the MFI scheme.

We also investigate the MFI accuracy in the presence of 1st PMD with a DGD ranging from 5 to 50 ps, and SOP angle of 5° and 25°. Fig. 8(a) and (b) show the MFI accuracy vs. DGD at SOP = 5° and 25°, respectively. It is observed that the MFI accuracy for PDM-BPSK, PDM-QPSK, PDM-8QAM, and PDM-32QAM is almost not affected by the increase of DGD as it remains greater than 98% at DGD = 45 and 35 ps for SOP = 5° and 25°, respectively. However, for PDM-16QAM and PDM-64QAM, the MFI accuracy drops below 70% at DGD = 50 ps. The average MFI accuracy result is presented in Fig. 8(c). It can be seen that the average MFI accuracy monotonically decreases as the effect of 1st PMD increases. For SOP = 25°, increasing DGD from 5 to 50 ps, decreases the average MFI accuracy from 97% to 81%, respectively. However, the average MFI accuracy reduces from 99% to 84% when SOP = 5°.

The fiber nonlinearity plays a significant role in optical fiber transmission systems, especially for long-haul networks, and its effects significantly limits the transmission distance. Because fiber nonlinearity is related to fiber length and transmitted power, we considered the fiber nonlinearity effect in terms of launched power within the range of −3 to 5 dBm at two different spans

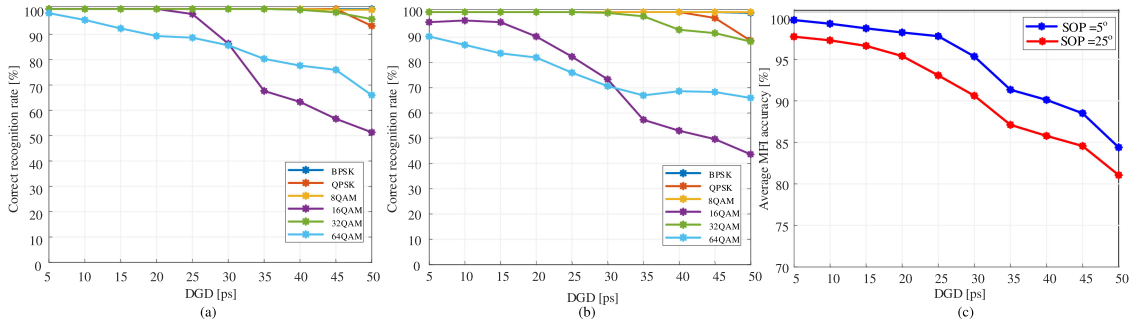

Fig. 8. (a) MFI accuracy vs. DGD at SOP = 5°, (b) MFI accuracy vs. DGD at SOP = 25°, and (c) average MFI accuracy vs. DGD at SOP = 5° and 25°.

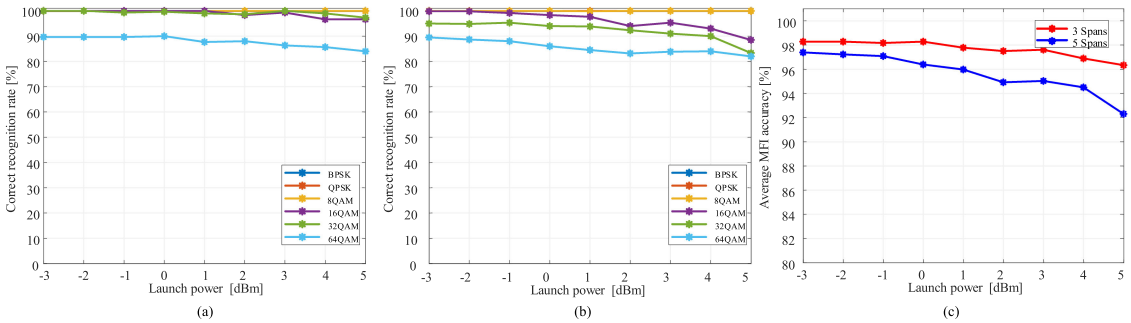

Fig. 9. (a) MFI accuracy vs. launch power at 3 spans, (b) MFI accuracy vs. launch power at 5 spans, and (c) average MFI accuracy vs. launch power at 3 and 5 spans.

(three and five spans). The length of each span is 80 km. For each span, we consider an optical amplifier with a noise figure of 5.5. It can be noticed that for three spans, the MFI for all modulation formats (except PDM-64 QAM) maintains accuracy greater than 97%. However, the classification accuracy for PDM-64QAM decreases to 90% when the transmitted power is above 0 dBm, as shown in Fig. 9(a). On the other hand, increasing the number of spans to five decreases the accuracy of the higher modulation formats such as PDM-16QAM, PDM-32QAM, and PDM-64QAM to 98%, 94%, and 87%, respectively (see Fig. 9(b) at launch power 0 dB). The average MFI accuracy for both three and five spans is depicted in Fig. 9(c). For the three spans, the average MFI remains unchanged ($\approx 98\%$) as the launch power increases from -3 dBm to 0 dBm and slightly decreases to around 96% as the launch power reaches 5 dBm. However, for five spans, the average MFI accuracy reduces from 97% to 92% when the launch power raises from 0 to 5 dBm.

Finally, we present results to compare the performance of CNN classifier employing 2D-IQH features with that of SVM classifier employing AH features, CDF features, and IQH features concatenated in the form of a 1D vector, where the average MFI accuracy versus OSNR ranging from 8 to 36 dB is presented for the middle subcarrier when $\eta = 1.1$. The results displayed in Fig. 10 show that the performance of 2D-IQH features with CNN outperform that of 1D-IQH features with SVM classifier. On the other hand, the 1D-IQH features with SVM achieve better accuracy than that of AH and CDF features. Further, the CDF features provide slightly better performance compared to that of AH features at higher OSNR values. For example, the average MFI accuracy of 2D-IQH with CNN reaches around

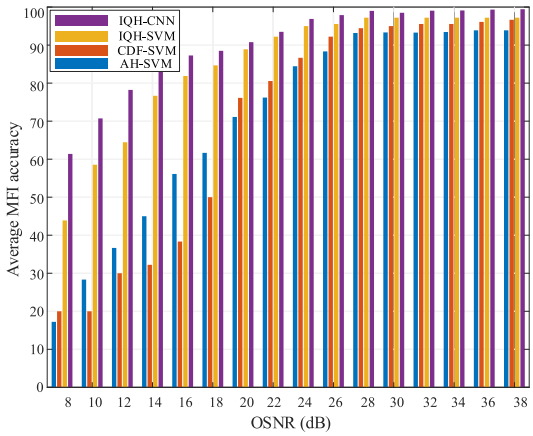

Fig. 10. Comparisons between MFI results of AH, CDF, and 1D-IQH with SVM classifier and 2D-IQH with CNN classifier.

98% and the 1D-IQH with SVM provides 96% accuracy at OSNR = 26 dB. However, CDF and AH features achieved only 92% and 88% accuracy, respectively. The reason for achieving a good performance for the IQH features compared to the AH and CDF features is due to the fact that IQH features are extracted from both amplitude and phase information of the signal. However, AH and CDF features exploit only the signal amplitude.

In what follows, we draw conclusions pertaining to the effects of channel interference, CD, PN, DGD, SOP, and fiber nonlinearity on the MFI performance. Here, we base our conclusions on the results obtained using the 2D-IQH with CNN classifier.

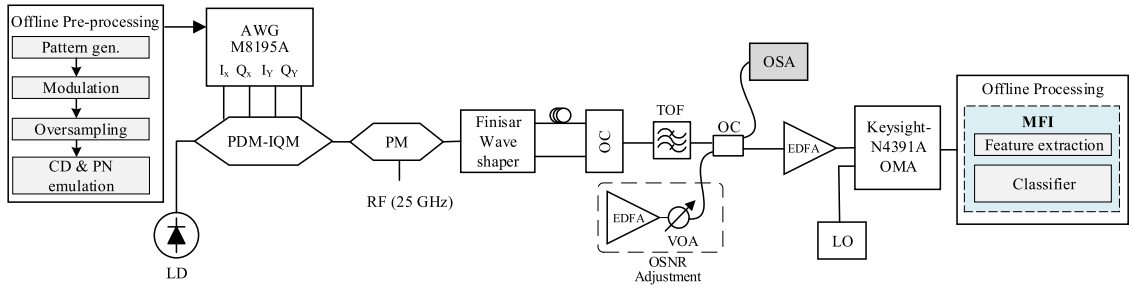

Fig. 11. Experimental setup of the proposed MFI in super-channel networks. LD: laser diode, CD: chromatic dispersion, PN: phase noise, AWG: arbitrary waveform generator, PDM-IQM: polarization division multiplexing-in-phase quadrature modulator, RF: radio frequency, PM: phase modulator, EDFA: Erbium-doped fiber amplifier, VOA: variable optical attenuator, OSNR: optical signal-to-noise ratio, TOF: tunable optical filter, OC: optical coupler, LO: local oscillator, OSA: optical signal analyzer, OMA: optical modulation analyzer, MFI: modulation format identification.

- For channel interference corresponding to $\eta = 1.1$, the classification accuracy of value $\geq$97% can be achieved for the side and middle subcarriers using PDM-BPSK, PDM-QPSK, PDM-8QAM, and PDM-32QAM schemes with OSNR $\geq$ 16 dB. The PDM-16QAM and PDM-64QAM schemes can achieve this classification rate if the side subcarrier is considered and the OSNR is set to value $\geq$ 22 dB. For the middle subcarrier, the PDM-16QAM and PDM-64QAM can achieve classification accuracies with rates $\geq$97% and $\geq$90%, respectively, at OSNR values $\geq$ 26 dB.
- For channel interference corresponding to $\eta = 1.2$, all modulation schemes almost maintain the same classification rate as the case $\eta = 1.1$, provided that the side subcarrier is being considered. This is also true for the middle subcarrier, except for PDM-64QAM, where the performance will degrade when η gets increased from 1.1 to 1.2 (e.g., there would be a 2 dB increase in OSNR at a classification rate of 90%).
- For channel interference corresponding to $\eta = 1.4$, the classification rate of two modulation schemes, PDM-16QAM and PDM-64QAM, will be greatly affected. For the side subcarrier, the classification rate can reach >90% when the OSNR $\geq$ 22 dB. However, the performance of PDM-16QAM and PDM-64QAM schemes is greatly reduced as it requires OSNR $\geq$ 30 dB to reach classification rates of 90% and 60%, respectively, when the middle subcarrier is being considered.
- For the middle subcarrier, channel interference corresponding to $\eta = 1.1$, CD (400 ps/nm) and PN (10 kHz), the PDM-BPSK, PDM-QPSK, PDM-8QAM, and PDM-32QAM schemes have 100% classification rate at OSNR=20 dB, while the performances of PDM-16QAM and PDM-64QAM have, respectively, 95% and 75% classification accuracy at OSNR = 30 dB. For CD=800 ps/nm and PN=1000 kHz, the PDM-BPSK, PDM-QPSK, and PDM-8QAM schemes need an extra 5 dB of OSNR to maintain the 100% classification accuracy, and the same amount is needed for the PDM-32QAM to reach and saturate at 95%. The performance of the other two schemes, the PDM-16QAM and PDM-64QAM, is greatly degraded ($\approx$60%) even at high OSNR values.
- For the middle subcarrier, channel interference corresponding to $\eta = 1.1$, PMD with a DGD ranging from 5 to 50 ps, and SOP angle of 5° and 25°, the average classification accuracy decreases to around 2% as SOP increases from 5° to 25°.
- For the middle subcarrier, channel interference corresponding to $\eta = 1.1$, launch power within the range -3 to 5 dBm, the classification accuracy almost remains unchanged in case of 3 spans fiber length. However, it decreases to 92% for 5 spans fiber length and launch power 5 dBm.

V. Experimental Validation

A proof-of-concept experiment setup is considered, as shown in Fig 11. In the experimental setup, the channel interference is chosen such that $\eta = 1.1$ and four PDM modulation schemes including PDM-BPSK, PDM-QPSK, PDM-8QAM, and PDM-16QAM at 20 Gbaud transmission speed are used in this demonstration. A low-linewidth laser source (i.e. NKT-Photonics) is used to generate a single optical carrier centered at 1550 nm. A pseudo-random binary sequence (PRBS) of length 2^{11}-1 is generated, mapped, and raised cosine shaped using Keysight M8195 A 64 GSa/s arbitrary waveform generator. The obtained multilevel electrical signals are used to drive a polarization division multiplexing IQ Mach-Zehnder modulator (PDM-IQM). The modulated carrier is then fed to a frequency comb source (FCS) constructed using a phase modulator (PM), RF signal source, and a 30 dB driver amplifier. This produces a set of optical subcarriers with channel spacing equal to the frequency of an RF signal source (i.e. 13 subcarriers in our case). In this work, a 25-GHz frequency spacing is considered. The output of FCS is fed into a wave shaper or wavelength selective switch (WSS) to select seven subcarriers. Since the subcarriers carry the same data, we separated the even and odd channels and applied an optical delay line to the even channels, then combined them together using an optical coupler (OC). A tunable optical filter (TOF) is adjusted to select one of the seven channels. To control the OSNR value, ASE noise is added and adjusted using an EDFA and an optical attenuator, respectively. The OSNR values are varied in the range of 8–22 dB and 12–26 dB for PDM-BPSK and PDM-QPSK, respectively, and 18–32 dB for PDM-8QAM and PDM-16QAM, with step of 2 dB. The optical subcarriers

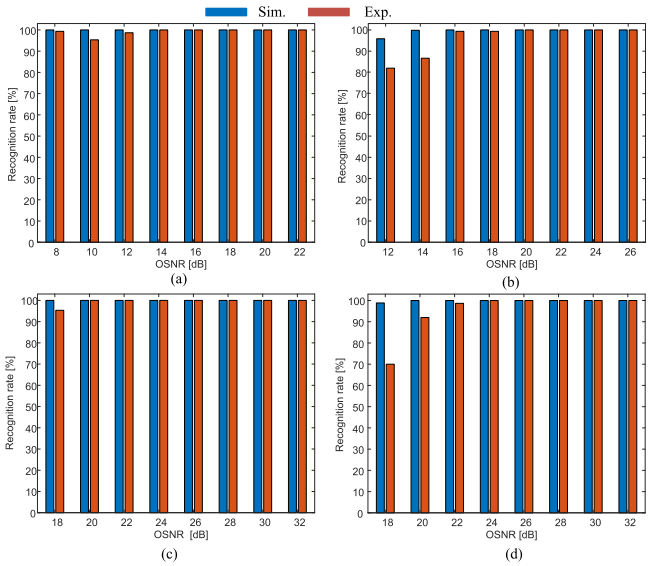

Fig. 12. Simulation vs experimental results of MFI at $\eta = 1.1$ for: (a) BPSK, (b) QPSK, (c) 8-QAM, and (d) 16-QAM.

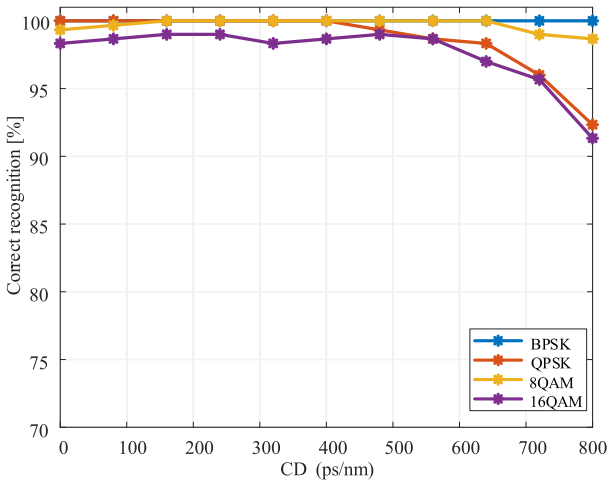

Fig. 13. MFI accuracy vs. CD .

and the ASE noise are combined together using an OC. The first output of the OC is connected to an optical spectrum analyzer (OSA), while a coherent optical receiver (N4391 A Keysight Optical Modulation Analyzer (OMA)) is connected to the other output. The obtained samples, taken after the sampling stage and before demodulation stage, are used to build the 2D-IQH. Finally, the MFI is performed using the CNN classifier.

We compared the performance of both simulation and experimental parts at $\eta = 1.1$. Fig. 12 shows a good agreement between both experimental and simulation results. In specific, both simulation and experimental results achieve high accuracies ($> 95\%$) for the four investigated schemes, at the high OSNR values. However, at high noise levels (i.e. 12–14 dB and 18–20 dB for PDM-QPSK and PDM-16QAM, respectively), the accuracy decreases owing to an increase in the difficulty to distinguish between the distorted IQH histograms of the two modulation formats. In addition, we study the MFI accuracy in the presence of CD ranging from 0 to 800 ps/nm when PN $= 100$ kHz. The results show that the MFI accuracy for all modulation formats $\geq 98\%$ at CD ≤ 560 ps/nm. Increasing the CD values above 560 ps/nm decreases the MFI accuracy for PDM-QPSK and PDM-16QAM, where the MFI accuracy reduces to 92% and 91%, respectively, when the CD reaches 800 ps/nm, as shown in Fig. 13.

VI. Conclusion

In this paper, we investigated the MFI over super-channel optical networks using a CNN classifier utilizing 2D-IQH features. The MFI is demonstrated using 7×20 Gbaud PDM-BPSK, PDM-QPSK, PDM-8QAM, PDM-16QAM, PDM-32QAM, and PDM-64QAM with OSNR range of 8-38 dB. The results showed that accurate identification accuracy can be achieved within the OSNR and channel interference ranges of practical systems. Further, the results showed that the MFI accuracy for side subcarriers outperforms that of middle subcarriers. Further, it is observed that the PDM-16QAM and PDM-64QAM signals are affected more by the presence of subcarriers interference compared to the other modulation formats. The investigation carried out in this work has also conducted an experimental demonstration to validate the simulation results, where it is observed that the two results are in good agreement with each other.

References

[1] I. Yaqoob, I. A. T. Hashem, Y. Mehmood, A. Gani, S. Mokhtar, and S. Guizani, "Enabling communication technologies for smart cities," *IEEE Commun. Mag.*, vol. 55, no. 1, pp. 112–120, Jan. 2017.

[2] M. Imran, P. M. Anandarajah, A. Kaszubowska-Anandarajah, N. Sambo, and L. Potí, "A survey of optical carrier generation techniques for terabit capacity elastic optical networks," *IEEE Commun. Surv. Tut.*, vol. 20, no. 1, pp. 211–263, Jan.–Mar. 2018.

[3] G. Bosco, V. Curri, A. Carena, P. Poggiolini, and F. Forghieri, "On the performance of Nyquist-WDM terabit superchannels based on PM-BPSK, PM-QPSK, PM-8QAM or PM-16QAM subcarriers," *J. Lightw. Technol.*, vol. 29, no. 1, pp. 53–61, 2011.

[4] X. Liu and S. Chandrasekhar, "Superchannel for next-generation optical networks," in *OFC*, San Francisco, CA, USA, 2014, pp. 1–33.

[5] P. J. Winzer, D. T. Neilson, and A. R. Chraplyvy, "Fiber-optic transmission and networking: The previous 20 and the next 20 years [Invited]," *Opt. Exp.*, vol. 26, no. 18, pp. 24190–24239, 2018.

[6] V. López *et al.*, "Elastic optical networks," *Architectures, Technol., Control*, Switzerland:Springer, 2016.

[7] E. Palkopoulou *et al.*, "Cognitive heterogeneous reconfigurable optical network: A techno-economic evaluation," in *Future Netw. Mobile Summit*, Stockholm, Sweden, 2013, pp. 1–10.

[8] W. Saif, M. A. Esmail, A. Ragheb, T. Alshawi, and S. Alshebeili, "Machine learning techniques for optical performance monitoring and modulation format identification: A survey," *IEEE Commun. Surv. Tut.*, vol. 22, no. 7, pp. 2839–2882, Oct.–Dec. 2020.

[9] Z. Zhao, A. Yang, P. Guo, and W. Tang, "A modulation format identification method based on amplitude deviation analysis of received optical communication signal," *IEEE Photon. J.*, vol. 11, no. 1, Feb. 2019, Art no. 7201807.

[10] Z. Zhao, A. Yang, and P. Guo, "A modulation format identification method based on information entropy analysis of received optical communication signal," *IEEE Access*, vol. 7, pp. 41492–41497, 2019.

[11] S. M. Bilal, G. Bosco, Z. Dong, A. P. T. Lau, and C. Lu, "Blind modulation format identification for digital coherent receivers," *Opt. Exp.*, vol. 23, no. 20, pp. 26769–26778, 2015.

[12] G. Liu, R. Proietti, K. Zhang, H. Lu, and S. J. B. Yoo, "Blind modulation format identification using nonlinear power transformation," *Opt. Exp.*, vol. 25, no. 25, pp. 30895–30904, 2017.

[13] J.-W. Kim and C.-H. Lee, "Modulation format identification of square and non-square M-QAM signals based on amplitude variance and OSNR," *Opt. Commun.*, vol. 474, 2020, Art. no. 126084.
[14] L. Jiang *et al.*, "An effective modulation format identification based on intensity profile features for digital coherent receivers," *J. Lightw. Technol.*, vol. 37, no. 19, pp. 5067–5075, 2019.
[15] J. Xie *et al.*, "A survey of machine learning techniques applied to software defined networking (SDN): Research issues and challenges," *IEEE Commun. Surv. Tut.*, vol. 21, no. 1, pp. 393–430, Jan.–Mar. 2019.
[16] E. Giacoumidis, A. Matin, J. Wei, N. J. Doran, L. P. Barry, and X. Wang, "Blind nonlinearity equalization by machine-learning-based clustering for single- and multichannel coherent optical OFDM," *J. Lightw. Technol.*, vol. 36, no. 3, pp. 721–727, 2018.
[17] W. S. Saif, A. M. Ragheb, T. Alshawi, and S. Alshebeili, "Optical performance monitoring in mode division multiplexed optical networks," *J. Lightw. Technol.*, vol. 39, no. 2, pp. 491–504, 2020.
[18] F. N. Khan, Q. Fan, C. Lu, and A. P. T. Lau, "An optical communication's perspective on machine learning and its applications," *J. Lightw. Technol.*, vol. 37, no. 2, pp. 493–516, 2019.
[19] T. S. R. Shen, K. Meng, A. P. T. Lau, and Z. Y. Dong, "Optical performance monitoring using artificial neural network trained with asynchronous amplitude histograms," *IEEE Photon. Technol. Lett.*, vol. 22, no. 22, pp. 1665–1667, Nov. 2010.
[20] Z. Yu *et al.*, "Loss weight adaptive multi-task learning based optical performance monitor for multiple parameters estimation," *Opt. Exp.*, vol. 27, no. 25, pp. 37041–37055, 2019.
[21] D. Wang *et al.*, "Intelligent constellation diagram analyzer using convolutional neural network-based deep learning," *Opt. Exp.*, vol. 25, no. 15, pp. 17150–17166, 2017.
[22] D. Wang *et al.*, "Modulation format recognition and OSNR estimation using CNN-based deep learning," *IEEE Photon. Technol. Lett.*, vol. 29, no. 19, pp. 1667–1670, Oct. 2017.
[23] R. A. Eltaieb *et al.*, "Efficient classification of optical modulation formats based on singular value decomposition and radon transformation," *J. Lightw. Technol.*, vol. 38, no. 3, pp. 619–631, 2020.
[24] R. Borkowski, D. Zibar, A. Caballero, V. Arlunno, and I. T. Monroy, "Stokes space-based optical modulation format recognition for digital coherent receivers," *IEEE Photon. Technol. Lett.*, vol. 25, no. 21, pp. 2129–2132, Nov. 2013.
[25] T. Bo, J. Tang, and C. Chan, "Modulation format recognition for optical signals using connected component analysis," *IEEE Photon. Technol. Lett.*, vol. 29, no. 1, pp. 11–14, Jan. 2017.
[26] L. Jiang *et al.*, "Blind density-peak-based modulation format identification for elastic optical networks," *J. Lightw. Technol.*, vol. 36, no. 14, pp. 2850–2858, 2018.
[27] W. Zhang *et al.*, "Identifying modulation formats through 2D stokes planes with deep neural networks," *Opt. Exp.*, vol. 26, no. 18, pp. 23507–23517, 2018.
[28] M. Hao *et al.*, "Stokes space modulation format identification for optical signals using probabilistic neural network," *IEEE Photon. J.*, vol. 10, no. 3, Jun. 2018, Art no. 7202213.
[29] A. Yi *et al.*, "Modulation format identification and OSNR monitoring using density distributions in stokes axes for digital coherent receivers," *Opt. Exp.*, vol. 27, no. 4, pp. 4471–4479, 2019.
[30] P. Isautier, J. Pan, R. DeSalvo, and S. E. Ralph, "Stokes space-based modulation format recognition for autonomous optical receivers," *J. Lightw. Technol.*, vol. 33, no. 24, pp. 5157–5163, 2015.
[31] W. S. Saif, A. M. Ragheb, H. E. Seleem, T. A. Alshawi, and S. A. Alshebeili, "Modulation format identification in mode division multiplexed optical networks," *IEEE Access*, vol. 7, pp. 156207–156216, 2019.
[32] S. Chandrasekhar, X. Liu, B. Zhu, and D. W. Peckham, "Transmission of a 1.2-tb/s 24-carrier no-guard-interval coherent OFDM superchannel over 7200-km of ultra-large-area fiber," in *Proc. 35th Eur. Conf. Opt. Commun.*, Vienna, Austria, 2009, pp. 1–2.
[33] ITU-T, "Spectral grids for WDM applications: DWDM frequency grid," Recommendation G.694.1, Sep. 2020.
[34] M. Mazur, J. Schröder, M. Karlsson, and P. A. Andrekson, "Joint superchannel digital signal processing for effective inter-channel interference cancellation," *J. Lightw. Technol.*, vol. 38, no. 20, pp. 5676–5684, 2020.
[35] E. Torrengo *et al.*, "Transoceanic PM-QPSK terabit superchannel transmission experiments at baud-rate subcarrier spacing," in *Proc. 36th Eur. Conf. Exhib. Opt. Commun.*, Turin, Italy, 2010, pp. 1–3.
[36] M. Mazur, J. Schröder, A. Lorences-Riesgo, T. Yoshida, M. Karlsson, and P. A. Andrekson, "12 b/s/Hz spectral efficiency over the C-band based on comb-based superchannels," *J. Lightw. Technol.*, vol. 37, no. 2, pp. 411–417, 2019.
[37] K. Igarashi *et al.*, "1.03-exabit/SKM super-Nyquist-WDM transmission over 7,326-km seven-core fiber," in *Proc. 39th Eur. Conf. Exhib. Opt. Commun.*, London, U.K., 2013, pp. 1–3.
[38] W. S. Saif, T. Alshawi, M. A. Esmail, A. Ragheb, and S. Alshebeili, "Separability of histogram based features for optical performance monitoring: An investigation using t-SNE technique," *IEEE Photon. J.*, vol. 11, no. 3, Jun. 2019, Art no. 7203012.
[39] X. Lin, Y. A. Eldemerdash, O. A. Dobre, S. Zhang, and C. Li, "Modulation classification using received signal's amplitude distribution for coherent receivers," *IEEE Photon. Technol. Lett.*, vol. 29, no. 21, pp. 1872–1875, Nov. 2017.
[40] C. M. Bishop, *Pattern Recognition and Machine Learning*. Berlin, Germany: Springer, 2006.
[41] S. Ioffe and C. Szegedy, "Batch normalization: Accelerating deep network training by reducing internal covariate shift," in *Proc. Int. Conf. Mach. Learn.*, 2015, pp. 448–456.